

## EXTENDED X-RAY EMISSION FROM A QUASAR-DRIVEN SUPERBUBBLE

JENNY E. GREENE<sup>1</sup>, DAVID POOLEY<sup>2</sup>, NADIA L. ZAKAMSKA<sup>3</sup>, JULIA M. COMERFORD<sup>4</sup>, AI-LEI SUN<sup>1</sup>*April 18, 2014; accepted by The Astrophysical Journal.*

## ABSTRACT

We present observations of extended, 20-kpc scale soft X-ray gas around a luminous obscured quasar hosted by an ultra-luminous infrared galaxy caught in the midst of a major merger. The extended X-ray emission is well fit as a thermal gas with a temperature of  $kT \approx 280$  eV and a luminosity of  $L_X \approx 10^{42}$  erg s<sup>-1</sup> and is spatially coincident with a known ionized gas outflow. Based on the X-ray luminosity, a factor of  $\sim 10$  fainter than the [O III] emission, we conclude that the X-ray emission is either dominated by photoionization, or by shocked emission from cloud surfaces in a hot quasar-driven wind.

## 1. INTRODUCTION

Black hole (BH) “feedback” is often invoked to regulate massive galaxy formation (e.g., Springel et al. 2005), but definitive examples of radiation from the quasar accretion disk driving powerful outflows are difficult to find (e.g., Moe et al. 2009). While clear evidence exists that powerful radio jets entrain warm gas and carry significant amounts of material out of their host galaxies (e.g., Nesvadba et al. 2006; Fu & Stockton 2009), the situation is far less clear for radio-quiet targets, which dominate the active galactic nucleus (AGN) population. In the past few years, we have identified a number of radio-quiet quasars with high intrinsic luminosities ( $M_B < -26.9$  mag) that show outflowing ionized gas on  $\sim 15$  kiloparsec (kpc) scales (Greene et al. 2011, 2012; Liu et al. 2013a,b; Hainline et al. 2013). In this paper, we present observations of hot X-ray gas that is aligned with a known 20-kpc-scale ionized gas bubble in the radio-quiet quasar SDSS J135646.10+102609.0 (SDSS J1356+1026 hereafter).

SDSS J1356+1026 is an on-going merger and ultra-luminous infrared galaxy (ULIRG) located at  $z=0.123$  ( $D_L = 568$  Mpc). The Northern nucleus hosts a luminous ( $L_{bol} \simeq 10^{46}$  erg s<sup>-1</sup>) obscured quasar that was originally discovered in the Sloan Digital Sky Survey (SDSS; York et al. 2000) based on its [O III]  $\lambda 5007$  emission (Zakamska et al. 2003; Reyes et al. 2008). The source was also flagged as a possible dual active nucleus, because of the presence of multiple velocity components in the SDSS spectrum, although that classification has been questioned (Liu et al. 2010; Fu et al. 2012).

Our interest here lies in the  $\sim 20$  kpc outflow that we discovered in long-slit observations with Magellan (Greene et al. 2009, 2012, Paper I hereafter). In our Magellan spectrum, we detect the line splitting that is characteristic of an expanding “bubble” (Figure 1). The shell region extends  $\sim 10$  kpc ( $\sim 4''$ ) to the South of the quasar hosted by the Northern nucleus. Equidistant from the Northern nucleus to the North are clumps of [O III] emission with comparable observed velocities to the bubble. We thus propose that we are observing an expanding bipolar super-bubble similar to those observed in many star-forming galaxies both with and without AGNs (e.g., Heckman et al. 1990; Rupke & Veilleux 2013).

## 2. A QUASAR-DRIVEN SUPERWIND?

As discussed in Paper I, based on the velocity splitting in our long-slit spectrum, we find that the bubble is expanding symmetrically about the Northern nucleus with deprojected velocities of  $\sim 1000$  km s<sup>-1</sup>. We infer that the outflow is driving a shell of ionized gas with a kinetic energy of ( $\sim 10^{44}$ – $10^{45}$  erg s<sup>-1</sup>), and we argue that accretion energy is the most likely energy source driving the outflow. We consider alternative sources to power the outflow, such as a relativistic jet or star formation in the host galaxy, and conclude that neither of these alternatives is energetic enough to produce the observed structures. Since SDSS J1356+1026 is radio-quiet, with a radio source that is unresolved by FIRST (Becker et al. 1995), we think it unlikely that a kpc-scale jet is driving the emission (although deeper radio data should be illuminating, Wrobel et al. in prep).

Converting the observed far-infrared (FIR) luminosity into a star formation rate of  $\sim 100 M_\odot$  yr<sup>-1</sup> yields a kinetic luminosity of  $\sim 10^{44}$  erg s<sup>-1</sup> (Leitherer & Heckman 1995; Veilleux et al. 2005), at the low end of our estimates. However, the star formation rate is likely far lower than this. Based on the gas surface density inferred from ALMA observations of CO in SDSS J1356+1026, combined with a fit to the far-infrared spectral energy distribution, we find a star formation rate that is  $< 21 M_\odot$  yr<sup>-1</sup> under a number of conservative assumptions (A. Sun et al. submitted). Furthermore, the high level of 8% optical polarization that we present in Paper I argues strongly that the AGN dominates the blue light at optical wavelengths.

Our preferred model, as described in Paper I, is that radiative energy from the AGN itself is driving a shocked wind into the interstellar medium of the galaxy, and further out into the intergalactic medium. The ionized gas we observe is just the frosting on a predominantly hot outflow (e.g., Faucher-Giguère & Quataert 2012; Zubovas & King 2012). In starburst galaxies, overlapping supernova remnants combine to create a hot expanding bubble of gas that, if sufficiently overpressured, will “break out” of the galaxy along the minor axis (e.g., Chevalier & Clegg 1985; Mac Low & McCray 1988). These hot winds can power kpc-scale superbubbles that are observable in the soft X-ray (e.g., Fabbiano et al. 1990; Strickland et al. 2004a,b), as well as ionized (e.g., Heckman et al. 1990; Rupke & Veilleux 2013), and neutral (e.g., Rupke et al. 2005) gas (see Veilleux et al. 2005, for a recent review). While we believe AGNs also drive hot winds (e.g., Choi et al. 2013), they are much more challenging to unambiguously detect in the X-rays, due to con-

<sup>1</sup> Department of Astrophysics, Princeton University, Princeton, NJ 08540<sup>2</sup> Department of Physics, Sam Houston State University, Huntsville, TX 77341, Eureka Scientific, Inc., 2452 Delmer Street Suite 100, Oakland, CA 94602<sup>3</sup> Center for Astrophysical Sciences, Department of Physics and Astronomy, Johns Hopkins University, Baltimore, MD 21218, USA<sup>4</sup> Department of Astrophysical and Planetary Sciences, University of Colorado, Boulder, CO 80309, USA

Table 1. X-ray Properties

Region	Net Counts [0.3–8 keV]	Spectral Model	Addl. $n_H$ ( $10^{20} \text{ cm}^{-2}$ )	$n_e$ $10^{-3} \text{ cm}^{-3}$	$kT$ [eV] or PL index	Unabs. $F_{0.3-8 \text{ keV}}$ ( $\text{erg cm}^{-2} \text{ s}^{-1}$ )	$L_{0.3-8 \text{ keV}}$ ( $10^{41} \text{ erg/s}$ )
Northern Clump	$6.2^{+3.0}_{-2.4}$	APEC	$< 16$	$1.2^{0.2}_{-0.4}$	$230^{+60}_{-50}$	$(2.7 \pm 1.1) \times 10^{-15}$	$1.0 \pm 0.4$
Southern Bubble	$14.2^{+4.2}_{-3.6}$	APEC	$< 7.5$	$1.5^{0.4}_{-0.3}$	$240^{+60}_{-50}$	$(4.7 \pm 1.6) \times 10^{-15}$	$1.8 \pm 0.6$
Total Non-nuclear	$53.0 \pm 7.6$	APEC	$< 20$	$2.4^{2.1}_{-0.2}$	$280^{+20}_{-60}$	$(1.8 \pm 0.5) \times 10^{-14}$	$7.0 \pm 1.9$
Northern Nucleus	$56.8 \pm 7.6$	PL	$< 2.4$	...	$1.8 \pm 0.2$	$(2.4 \pm 0.7) \times 10^{-14}$	$9.3 \pm 2.7$

Note. — All confidence intervals are  $1\sigma$ .  $n_e$  calculations assume both the clump and bubble regions have one-third the volume of the total. See text for details of spectral models.

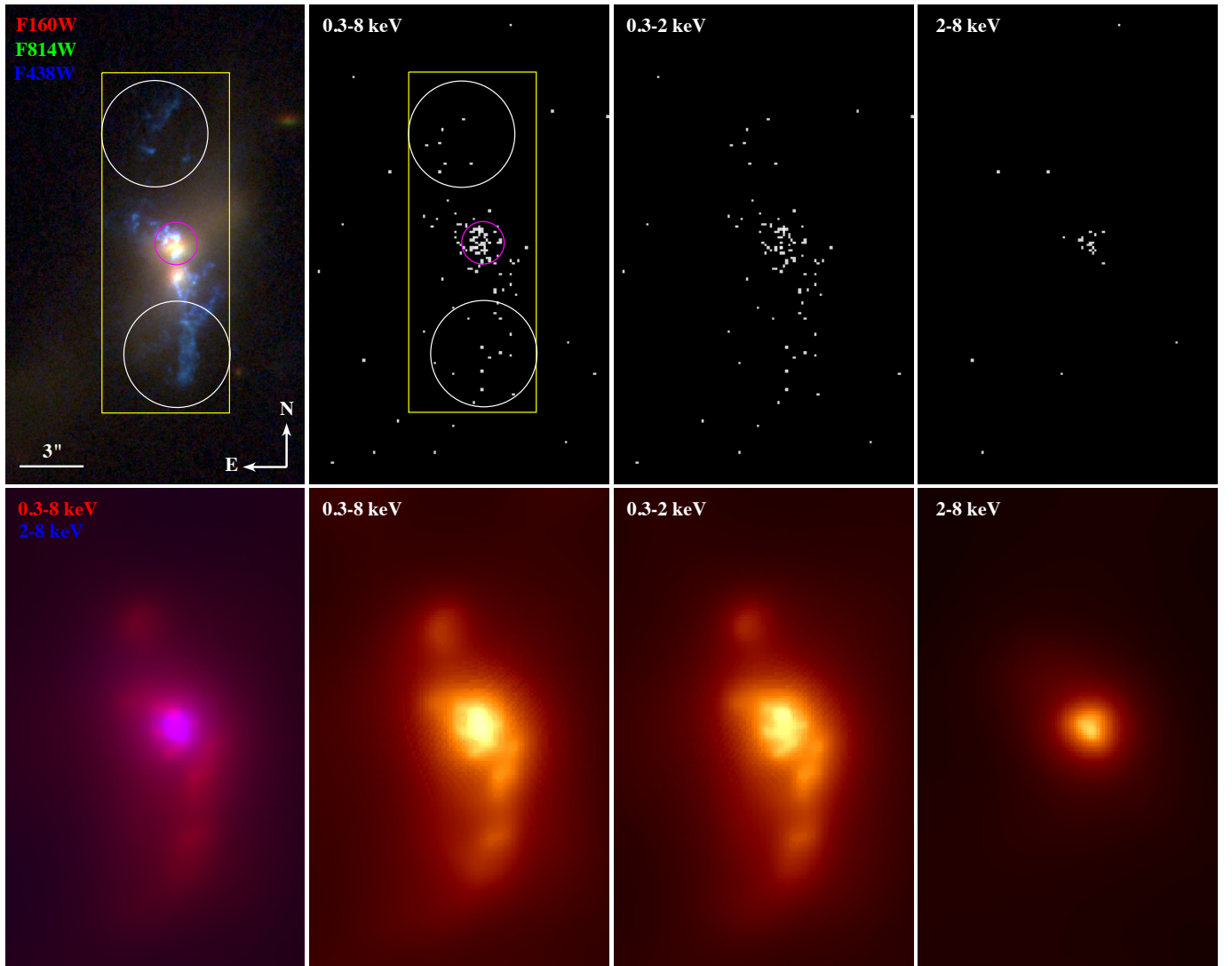


FIG. 1.— *HST* (top left) and *Chandra* views of SDSS J1356+1026. In the top-left panel, we show the three-band WFC3 composite image. The extended blue/green light is dominated by line emission, while the red is stellar tidal features. The orientation of all images has North up and East to the left, and the extraction regions for the bubble and clumps are indicated by white circles, while the total extraction region is shown as a yellow rectangle and the North nucleus extraction region is the magenta circle. In the remaining top panels, we show the X-ray maps in the 0.3–8, 0.3–2, and 2–8 keV energy ranges. In the bottom panels, we show adaptively smoothed images to guide the eye, although we caution against overinterpreting these.

fusion from photoionization (e.g., Bianchi et al. 2006; Wang et al. 2011), star formation (e.g., Wang et al. 2009), and collisional ionization (e.g., Paggi et al. 2012). SDSS J1356+1026 provides an exciting opportunity to explore the nature of X-rays from an AGN-driven superbubble on  $\sim 20$  kpc scales.

### 3. X-RAY OBSERVATIONS AND ANALYSIS

J. Comerford et al. in prep. observed SDSS J1356+1026 for 19.8 ks on 2012 March 31 (ObsID 13951) with the Advanced CCD Imaging Spectrometer (ACIS). The data were taken in timed-exposure mode with an integration time of 3.14 s per frame, and the telescope aim point was on the back-side illuminated S3 chip. The data were telemetered to the ground in faint mode.

Reduction was performed using the CIAO 4.5 software (Fruscione et al. 2006) provided by the *Chandra* X-ray Center. The data were reprocessed with the `chandra_repro` script using the CALDB 4.5.8 set of calibration files (gain maps, quantum efficiency, quantum efficiency uniformity, effective area). The data were filtered using standard event grades and excluding both bad pixels and software-flagged cosmic-ray events. No intervals of strong background flaring were found.

We use  $5''$  diameter regions (see Fig. 1) to extract counts from the northern clump region and the southern bubble region, and we use a  $2'$  source-free region to the southwest to estimate the background contribution, which is small (less than one count for the clump and bubble regions). Finally, as an upper limit to the extended diffuse X-ray counts, we extract all counts within a  $6 \times 16''$  region centered on the Northern nucleus, excluding a  $1''$  region around the Northern nucleus itself. We present the extracted counts in each region in Table 1. Because there are only a small number of counts in each source region, we use the Bayesian method of Kraft et al. (1991) to estimate the uncertainties on the net counts.

Spectra were extracted from the clump, bubble, Northern nucleus, and total non-nuclear regions, along with a background spectrum from the  $2'$  background region. The unbinned spectra were fit in Sherpa (Freeman et al. 2001) using Cash (1979) statistics. The spectral model for the clump, bubble, and total extended regions was an absorbed (Wilms et al. 2000) thermal plasma model (APEC) at the redshift of the host galaxy. The confidence intervals for the parameters are determined using the task `conf` within Sherpa, taking into account the presence of several variables in the fit.

We fix the abundances to their solar values for our fiducial fit. In Figure 2, we show the Cash statistic minimum for each fitted parameter:  $kT$ , normalization, which scales with gas density, and absorbing column  $n_H$ . Each parameter of interest  $p$  is stepped through a grid of 100 points between the limits shown, and  $p$  is held fixed while all other parameters are allowed to vary to find the best fit at this value of  $p$ . The Cash statistic of this new best fit is plotted at each value, showing that we find clearly defined minima in both the temperature  $kT$  and the normalization. The two-dimensional confidence contours are created in a similar way, and plotted at the  $1, 2, 3 \sigma$  levels. Within the context of a thermal plasma model,  $kT$  is very low no matter the value of the other parameters. This low temperature can be seen from the X-ray counts themselves; the majority of the extended counts are below 1 keV. It may be that the assumption of solar abundances is incorrect; Nardini et al. (2013) find abundances closer to half the solar value in the X-ray halo of NGC 6240, perhaps with a component of one-tenth solar metallicity

as well. As an additional check, we also fit models with abundances one-half and one-tenth solar and find differences in the best-fit  $kT$  only at the  $< 10\%$  level.

The absorbing column consists of two components, one fixed at the Milky Way value of  $n_H = 1.9 \times 10^{20} \text{ cm}^{-2}$  in the direction of SDSS J1356+1026 (Dickey & Lockman 1990), and an additional component at the redshift of SDSS J1356+1026. No additional absorption was required, with  $1 \sigma$  upper limits given in Table 1. We calculate the unabsorbed fluxes from the best-fit models. To estimate the uncertainties in the flux, we used the `sample_energy_flux` command in Sherpa to obtain 10 000 samples of the energy flux, taking into account the uncertainties in all of the spectral parameters. The uncertainties are dominated by statistical uncertainties at these flux levels, and we use the standard deviations of these sets of samples as the uncertainties for the fluxes (Table 1). While we are fitting a low total number of counts, the fact that the photons are all at very low energies rules out both high temperatures and large absorbing columns. The agreement between all three region fits provides extra support for our methodology and derived uncertainties.

The North nucleus itself was fit with an absorbed power-law model [with slope  $\Gamma$ ,  $N(E) \propto E^\Gamma$ ] with the same absorption components as above. Surprisingly, we find no evidence for intrinsic absorption in the X-ray spectrum, although the source is classified as a narrow-line AGN in the optical and we have detected 8% polarization, usually a tell-tale sign of an obscured AGN (Paper I). The best-fit power-law slope is  $1.8 \pm 0.2$ , and the column-density settled at the minimum value, with a  $1 \sigma$  upper uncertainty of  $1.8 \times 10^{20} \text{ cm}^{-2}$ . This is a standard power-law slope for local unobscured Seyfert galaxies (e.g., Jin et al. 2012). Perhaps the source is similar to “changing-look” AGNs, which transition from Compton-thick to thin, but are obscured in the optical (e.g., Risaliti et al. 2005).

#### 3.1. Optical Line Emission

In determining the nature of the X-rays, we compare their morphology and luminosity of the warm ionized gas, as traced by [O III] in our long-slit Magellan data (Greene et al. 2009) and three-band *HST*/WFC3 imaging in F435W (*B*-band), F814W (*I*-band), and F160W (*H*-band) from Comerford et al. in prep. The total [O III] luminosity within our slit is  $\sim 10^{43} \text{ erg s}^{-1}$ . Because the line emission is spatially extended, this estimate is strictly a lower limit. Given that the majority of the emission visible in the *HST* images align with our slit, we expect we are within a factor of two to three of the total [O III] emission. From our long-slit data, we determine that the nuclear emission within  $1''$  of the North nucleus accounts for only  $\sim 10\%$  of the total flux, a small fraction compared to the larger (and more uncertain) aperture corrections. Thus, we consider the extended [O III] emission to have a luminosity of  $L_{[\text{O III}]} \approx 10^{43} \text{ erg s}^{-1}$ . We trace the overall line morphology using the *HST*/WFC3 F438W and F814W images, because the line emission has high enough equivalent width to be observed in a broad-band image (Figure 1). The morphology of the X-rays matches that of the line emission, to the extent we can tell from these relatively shallow observations.

### 4. DISCUSSION

We find a total soft X-ray luminosity of  $5 - 9 \times 10^{41} \text{ erg s}^{-1}$  with a best-fit temperature of  $\sim 280 \text{ eV}$ , and a total [O III] luminosity in the extended component of  $\sim 10^{43} \text{ erg s}^{-1}$ . Thus the extended X-ray emission is roughly an order of magnitude

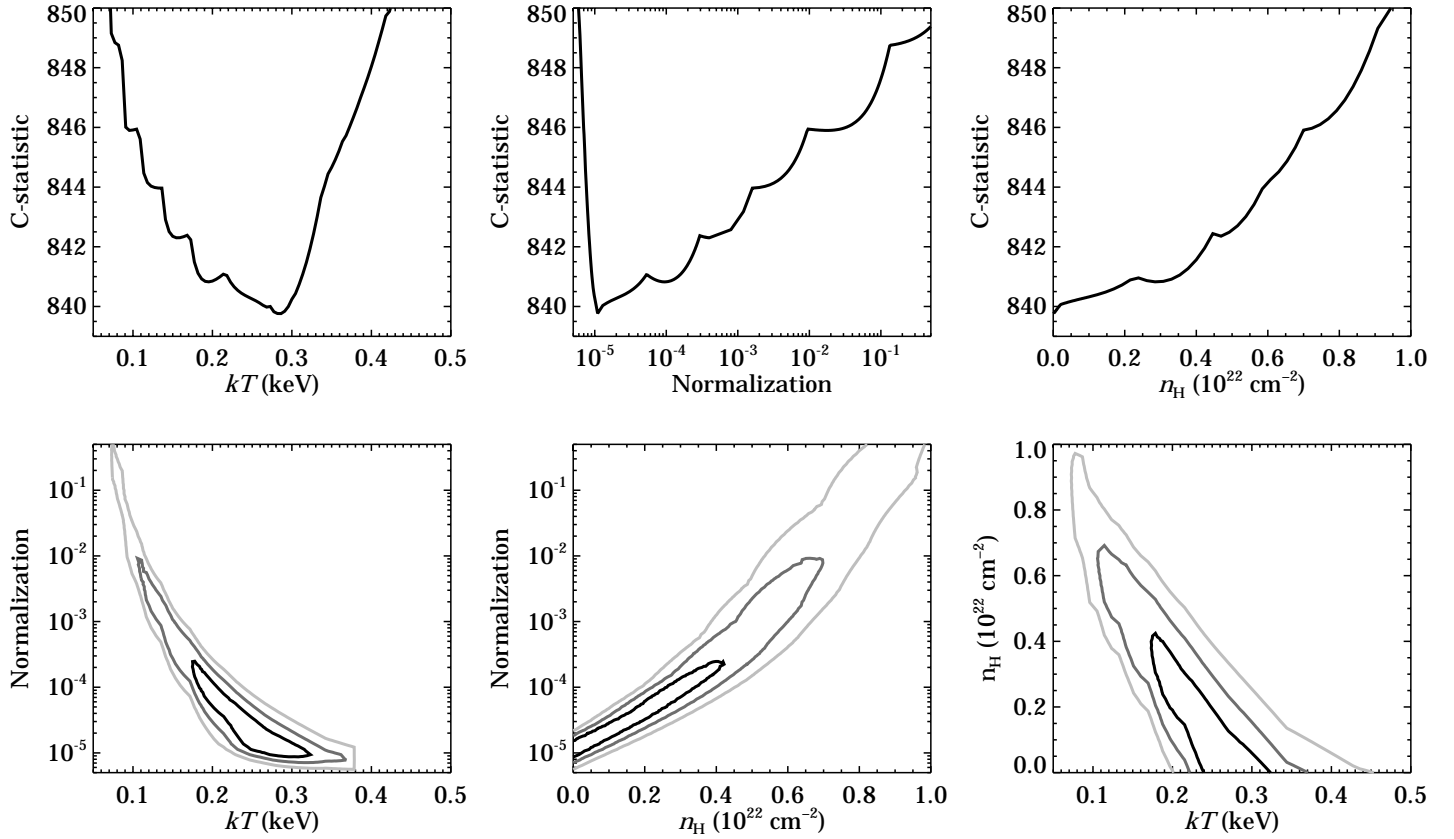


FIG. 2.— *Top*: Cash statistic for each parameter of interest derived by fixing the latter and allowing all other parameters to vary freely. The normalization is defined to be  $(10^{-14}/4\pi[D_A(1+z)]^2) \int n_e n_H dV$  where  $D_A$  is the angular diameter distance to the source in cm and  $n_e$  and  $n_H$  are the electron and hydrogen density in  $\text{cm}^{-3}$ . There is a distinct minimum in both  $kT$  and normalization. *Bottom*: Two-dimensional confidence contours derived in a similar fashion, by fixing the two parameters of interest over a grid and then allowing the fit to converge at the best Cash statistic. The contour levels connect the 1  $\sigma$ , 2  $\sigma$ , and 3  $\sigma$  regions where the Cash statistic has a value 2.30, 6.18, and 11.83 higher than the overall best model.

fainter than the extended [O III] emission. We discuss below the possible origins of the overwhelmingly soft extended X-ray emission. The prime suspects, in order from least to most probable, are electron scattering, superwind-driven shocks, and photoionization. We note that McDowell et al. (2003) also suggest merger-driven shocks as the heating mechanism of the X-ray emitting gas in Arp 220 (see also Nardini et al. 2013, for similar arguments about NGC 6240). However, as pointed out by Grimes et al. (2005), non-starbursting mergers do not appear to show similar X-ray halos, strongly suggesting winds over mergers as the heating mechanism.

#### 4.1. Electron scattering

Electron scattering of the AGN continuum could provide X-ray photons, but cannot account for the observations. For one thing, scattering would not change the hard spectral slope intrinsic to the AGN, so cannot explain the very soft extended X-rays. Secondly, the scattering efficiency is too low to account for the observed luminosity. If we assume that the intrinsic UV luminosity is  $\sim$  twice that of the infrared bump in Paper I (e.g., Richards et al. 2006), we can estimate an intrinsic  $\nu L_\nu[2000 \text{ \AA}] = 3 \times 10^{45} \text{ erg s}^{-1}$ . Assuming that all UV emission is due to electron-scattered light from the nucleus places an upper limit on the electron-scattering efficiency of 3% (much less so if there is a contribution from dust). Since electron-scattering is wavelength independent and dust scattering is negligible at X-ray wavelengths, and given the luminosity of the North nucleus  $L_X = (9 \pm 3) \times 10^{41} \text{ erg s}^{-1}$ , an upper limit to the scattered X-ray luminosity is  $\ll 3\% \times (9 \pm 3) \times 10^{42} \text{ erg s}^{-1}$ , or  $L_X/L_{[\text{O III}]} \ll 0.003$ , much lower than the observed X-ray luminosity. Finally, the amount of scattering is constrained by the amount of line emission. From Zakamska et al. (2005), if we take  $n_e \sim 100 \text{ cm}^{-3}$  and  $d \sim 5 \text{ kpc}$ , we expect  $L_X/L_{[\text{O III}]} \approx 0.005$ , also lower than the ratio of  $\sim 0.1$  that is observed.

#### 4.2. Superwind

Perhaps the most exciting possibility is that we are detecting shocked gas associated with a wide-angle, quasar-driven wind (e.g., Faucher-Giguère & Quataert 2012; Choi et al. 2013). Such a super-wind would have similar properties to those blown by starbursts, but the gas would be heated by the accreting black hole rather than star formation.

To estimate the expected luminosity in the soft X-rays from a superwind, we follow Heckman et al. (1996) and assume that the expanding bubble of hot gas behaves like a supernova remnant, with negligible radiative losses, in order to translate our estimated mechanical luminosity of  $L_{\text{mech}} \approx 10^{44} - 10^{45} \text{ erg s}^{-1}$  into an expected X-ray luminosity (see also Chevalier & Clegg 1985). Their derived relationship is:

$$L_X \approx 3.1 \times 10^{40} L_{\text{mech},43}^{33/35} n_{e,-2}^{17/35} t_7^{19/35} \text{ erg s}^{-1}, \quad (1)$$

where  $L_{\text{mech}}$  is in units of  $10^{43} \text{ erg s}^{-1}$ ,  $n_{e,-2}$  is the density in units of  $10^{-2} \text{ cm}^{-3}$  and  $t_7$  is the estimated age of the bubble in units of  $10^7 \text{ yr}$ . The observed X-ray luminosity has  $L_X \approx f n_e n_H V \epsilon$ , with APEC calculating the emissivity  $\epsilon$ ,  $f$  the volume filling factor,  $n_e \approx n_H$ , and the volume  $V$  assumed to be a cylinder with length 20 kpc and radius 2 kpc. From the APEC spectral model, we find a best-fit electron density of  $n_e \approx 0.002 \text{ cm}^{-3}$ . We emphasize that the normalization is poorly constrained from these data (Figure 2, but it is interesting to perform this estimate

nevertheless. Taking  $t \approx 10^7 \text{ yr}$  and the range of mechanical luminosity from Paper I, we find  $L_X \approx 2 \times 10^{41} - 10^{42} \text{ erg s}^{-1}$ , in agreement with what we observe. The corresponding X-ray emitting gas mass is  $M_X \approx 10^{10} f^{1/2} M_\odot$ , with a total thermal energy of  $E = PV = 2n_e kTV \approx 1.3 \times 10^{58} f^{1/2} \text{ erg}$ , or  $\dot{E} = 3 \times 10^{43} f^{1/2} \text{ erg s}^{-1}$ . The uncertainties in these calculations are quite large, due to the uncertainties in the spectral fitting and the unknown volume and volume filling factor. However, the kinetic luminosity needed to power the X-ray outflow is within a factor of three of what we inferred from the ionized gas outflow.

On the other hand, models of superwinds suggest that the wind is powered by far more tenuous and hotter gas than we observe here,  $\sim 10^7 \text{ K}$  for starbursts (Strickland & Stevens 2000) and perhaps even hotter for AGN (e.g., Zubovas & King 2012). In that case, the soft X-rays may come from the surfaces of clouds as they are shocked by the wind, and the X-ray luminosity cannot be inferred directly from the mechanical energy estimates. However, we can still phenomenologically compare the X-rays that we observe with other known superwinds.

Most of the bolometric luminosity of starbursts and obscured quasars is radiated at infrared wavelengths. Therefore, it is useful to compare extended soft X-ray to total infrared flux ratios for a variety of wind-driving systems. In starburst galaxies over a wide range in mass, including ULIRGs, Grimes et al. (2005) find  $f_X/f_{\text{FIR}} \approx 10^{-4}$ . The ratio in SDSS J1356+1026 is consistent with this value. Likewise the size scales as one might naively expect from the infrared luminosity. The one way in which the X-ray gas observed here differs significantly from that observed in starbursts is the temperature. Most of the ULIRGs in the Grimes et al. sample have temperatures of  $kT \approx 600 - 800 \text{ eV}$ , as compared with the  $kT \approx 280 \text{ eV}$  observed here. Based on our fitting, we rule out a temperature of 600 eV at greater than  $10 \sigma$  confidence. This low inferred temperature may be a clue that we are instead seeing photoionized gas.

#### 4.3. Photoionization

Since we know that the central AGN is photoionizing gas on large scales, and because of the correspondence in morphology between the soft X-ray and warm ionized gas, we lastly consider the possibility that what appears as X-ray continuum at our low spectral resolution is actually composed of photoionized line emission. Detailed analysis of the extended X-ray emission around local Seyfert galaxies has found strong evidence that the soft X-ray emission is dominated by photoionization on large scales (Bianchi et al. 2006; Wang et al. 2011) and comprised predominantly of line emission (e.g., Sambruna et al. 2001), although on galaxy scales collisional ionization is also important (e.g., Paggi et al. 2012; Wang et al. 2014). Based on these works, the  $L_X/L_{[\text{O III}]}$  ranges from 0.1–0.3, and is fairly constant with radius. The relatively low temperatures of  $kT \approx 280 \text{ eV}$  are consistent with the temperatures that result from thermal fits to other Seyfert galaxies. Also, the observed ratio of X-ray to [O III] luminosity of 0.05–0.1 is consistent with expectations from photoionized gas (and is identical to that seen in NGC 4051 by Wang et al. 2011). Furthermore, the orientation of the X-ray emission (N-S) aligns with the direction of quasar illumination inferred from the position angle in polarimetric observations (Paper I).

## 5. SUMMARY

We have detected soft X-rays from an expanding bubble of warm ionized gas in the obscured quasar and ULIRG SDSS J1356+1026. We discuss various origins for the X-ray emission, concluding that the most probable are photoionization and/or shocks from a quasar-driven superwind. To determine the real origin of this emission requires deeper X-ray observations. As in Bianchi et al. (2006), we hope to distinguish between the spectrum of a thermally emitting gas, as expected in the wind picture, from the line-dominated spectrum expected if photoionization excites the gas. In the wind picture, we expect that there is a hotter and more tenuous wind component to search for, although the expected temperature and luminosity is

quite model dependent. In addition, the morphology of the soft X-rays will provide further clues to its origin. In the hot wind scenario, the X-rays will be uniformly distributed within the bubbles, whereas in the photoionization scenario, the X-rays will trace the distribution of [O III] emission in the bubbles.

We thank the referee for a prompt and useful report. We thank C. A. Faucher-Giguere, E. Quataert, and J. P. Ostriker for inspiring us to look for X-ray emission from SDSS J1356+1026. J. M. C. acknowledges support from *Chandra* grant G02-13130.

## REFERENCES

- Becker, R. H., White, R. L., & Helfand, D. J. 1995, *ApJ*, 450, 559  
 Bianchi, S., Guainazzi, M., & Chiaberge, M. 2006, *A&A*, 448, 499  
 Cash, W. 1979, *ApJ*, 228, 939  
 Chevalier, R. A., & Clegg, A. W. 1985, *Nature*, 317, 44  
 Choi, E., Naab, T., Ostriker, J. P., Johansson, P. H., & Moster, B. P. 2013, *MNRAS*, submitted (arXiv:1308.3719)  
 Dickey, J. M., & Lockman, F. J. 1990, *ARA&A*, 28, 215  
 Fabbiano, G., Heckman, T., & Keel, W. C. 1990, *ApJ*, 355, 442  
 Faucher-Giguère, C.-A., & Quataert, E. 2012, *MNRAS*, 425, 605  
 Freeman, P., Doe, S., & Siemiginowska, A. 2001, in *Society of Photo-Optical Instrumentation Engineers (SPIE) Conference Series*, Vol. 4477, Society of Photo-Optical Instrumentation Engineers (SPIE) Conference Series, ed. J.-L. Starck & F. D. Murtagh, 76–87  
 Fruscione, A., et al. 2006, in *Society of Photo-Optical Instrumentation Engineers (SPIE) Conference Series*, Vol. 6270, Society of Photo-Optical Instrumentation Engineers (SPIE) Conference Series  
 Fu, H., & Stockton, A. 2009, *ApJ*, 690, 953  
 Fu, H., Yan, L., Myers, A. D., Stockton, A., Djorgovski, S. G., Aldering, G., & Rich, J. A. 2012, *ApJ*, 745, 67  
 Greene, J. E., Zakamska, N. L., Ho, L. C., & Barth, A. J. 2011, *ApJ*, 732, 9  
 Greene, J. E., Zakamska, N. L., Liu, X., Barth, A. J., & Ho, L. C. 2009, *ApJ*, 702, 441  
 Greene, J. E., Zakamska, N. L., & Smith, P. S. 2012, *ApJ*, 746, 86  
 Grimes, J. P., Heckman, T., Strickland, D., & Ptak, A. 2005, *ApJ*, 628, 187  
 Hainline, K. N., Hickox, R., Greene, J. E., Myers, A. D., & Zakamska, N. L. 2013, *ApJ*, 774, 145  
 Heckman, T. M., Armus, L., & Miley, G. K. 1990, *ApJS*, 74, 833  
 Heckman, T. M., Dahlem, M., Eales, S. A., Fabbiano, G., & Weaver, K. 1996, *ApJ*, 457, 616  
 Jin, C., Ward, M., & Done, C. 2012, *MNRAS*, 422, 3268  
 Kraft, R. P., Burrows, D. N., & Nousek, J. A. 1991, *ApJ*, 374, 344  
 Leitherer, C., & Heckman, T. M. 1995, *ApJS*, 96, 9  
 Liu, G., Zakamska, N. L., Greene, J. E., Nesvadba, N. P. H., & Liu, X. 2013a, *MNRAS*, 430, 2327  
 —. 2013b, *MNRAS*  
 Liu, X., Shen, Y., Strauss, M. A., & Greene, J. E. 2010, *ApJ*, 708, 427  
 Mac Low, M.-M., & McCray, R. 1988, *ApJ*, 324, 776  
 McDowell, J. C., et al. 2003, *ApJ*, 591  
 Moe, M., Arav, N., Bautista, M. A., & Korista, K. T. 2009, *ApJ*, 706, 525  
 Nardini, E., Wang, J., Fabbiano, G., Elvis, M., Pellegrini, S., Risaliti, G., Karovska, M., & Zezas, A. 2013, *ApJ*, 765, 141  
 Nesvadba, N. P. H., Lehnert, M. D., Eisenhauer, F., Gilbert, A., Tecza, M., & Abuter, R. 2006, *ApJ*, 650, 693  
 Paggi, A., Wang, J., Fabbiano, G., Elvis, M., & Karovska, M. 2012, *ApJ*, 756, 39  
 Reyes, R., Zakamska, N. L., Strauss, M. A., Green, J., Krolik, J. H., Shen, Y., Richards, G. T., Anderson, S. F., & Schneider, D. P. 2008, *AJ*, 136, 2373  
 Richards, G. T., et al. 2006, *ApJS*, 166, 470  
 Risaliti, G., Elvis, M., Fabbiano, G., Baldi, A., & Zezas, A. 2005, *ApJ*, 623, L93  
 Rupke, D. S., Veilleux, S., & Sanders, D. B. 2005, *ApJ*, 632, 751  
 Rupke, D. S. N., & Veilleux, S. 2013, *ApJ*, 768, 75  
 Sambruna, R. M., Netzer, H., Kaspi, S., Brandt, W. N., Chartas, G., Garmire, G. P., Nousek, J. A., & Weaver, K. A. 2001, *ApJ*, 546, L13  
 Springel, V., Di Matteo, T., & Hernquist, L. 2005, *MNRAS*, 361, 776  
 Strickland, D. K., Heckman, T. M., Colbert, E. J. M., Hoopes, C. G., & Weaver, K. A. 2004a, *ApJS*, 151, 193  
 —. 2004b, *ApJ*, 606, 829  
 Strickland, D. K., & Stevens, I. R. 2000, *MNRAS*, 314, 511  
 Veilleux, S., Cecil, G., & Bland-Hawthorn, J. 2005, *ARA&A*, 43, 769  
 Wang, J., Fabbiano, G., Elvis, M., Risaliti, G., Mazzarella, J. M., Howell, J. H., & Lord, S. 2009, *ApJ*, 694, 718  
 Wang, J., et al. 2011, *ApJ*, 742, 23  
 —. 2014, *ApJ*, 781, 55  
 Wilms, J., Allen, A., & McCray, R. 2000, *ApJ*, 542, 914  
 York, D. G., et al. 2000, *AJ*, 120, 1579  
 Zakamska, N. L., et al. 2003, *AJ*, 126, 2125  
 —. 2005, *AJ*, 129, 1212  
 Zubovas, K., & King, A. 2012, *ApJ*, 745, L34